RSC Advances

PAPER

View Article Online
View Journal | View Issue

Cite this: *RSC Adv.*, 2023, **13**, 7267

Design of blueberry anthocyanin/TiO_2 composite layer-based photoanode and N-doped porous blueberry-derived carbon-loaded Ni nanoparticle-based counter electrode for dye-sensitized solar cells†

Xiang Qin,‡[ab] Jingjing Liu,‡[ab] Genhui Teng,[ab] Baorui Liu,[ab] Yanhui Xie,[ab] Lin Ma[ab] and Dongying Hu *[ab]

Received 26th January 2023
Accepted 21st February 2023

DOI: 10.1039/d3ra00545c

rsc.li/rsc-advances

P25/PBP (TiO_2, anthocyanins) prepared by combining PBP (blueberry peels) with P25, and N-doped porous carbon-supported Ni nanoparticles (Ni@NPC-*X*) prepared using blueberry-derived carbon were used for the application as photoanode and the counter electrode, respectively, in dye-sensitized solar cells (DSSCs) to create a new perspective for blueberry-based photo-powered energy systems. PBP was introduced into the P25 photoanode and carbonized to form a C-like structure after annealing that improved its adsorption capacity for N719 dye, contributing a 17.3% higher power conversion efficiency (PCE) of P25/PBP-Pt (5.82%) than that of P25-Pt (4.96%). The structure of the porous carbon changes from a flat surface to a petal-like structure due to the N doping by melamine, and the specific surface area increases. N-doped three-dimensional porous carbon supported the loading and reduced the agglomeration of Ni nanoparticles, reducing the charge transfer resistance, and providing a fast electron transfer path. The doping of Ni and N on the porous carbon worked synergistically to enhance the electrocatalytic activity of the Ni@NPC-*X* electrode. The PCE of the DSSCs assembled by Ni@NPC-1.5 and P25/PBP was 4.86%. Also, the Ni@NPC-1.5 electrode exhibited 116.12 F g^{-1} and a capacitance retention rate of 98.2% (10 000 cycles), further confirming good electrocatalysis and cycle stability.

1 Introduction

The continuous progress of urbanization has put forward new demands and higher requirements for energy demand and sustainable development.[1] Priority selection of clean energy is undoubtedly the right direction to solve the above problems. Solar cells can effectively convert clean-energy solar radiation into one of the most convenient forms of electricity, highlighting its dominant position.[2,3] Among them, the design of dye-sensitized solar cells (DSSCs) is inspired by nature and then applied to the energy supply of the human environment through simple utilization.[4] For DSSCs, the research on photoanodes and counter-electrode materials has never faded out of the research field due to its dominant position.[5–7]

Taking the common titanium dioxide (TiO_2) photoanode as basic, great effects have been adopted in improving the photoanode by means of micro–nano structure design, multiple heterogeneous doping, physical/chemical modification, and other methods. Compared with transition metal element doping and precious metal deposition, carbon material doping has attracted widespread attention due to its wide material sources and adjustable structure, including graphitic carbon nitride,[8,9] carbon nanotubes, porous carbon, and graphite.[10] Lu *et al.* doped hierarchical carbon nanofibers (CFs) in TiO_2 and the photoelectron migration in the photoanode was improved.[11] Khan *et al.* synthesized cobalt-reduced graphene oxide Co-doped TiO_2 nanoparticles by the sol–gel method, which effectively improved the electron transport ability of the Co/rGO-TiO_2 photoanode.[12] The doping of carbon materials in the TiO_2 layer is a very effective method to improve the electron collection characteristics of DSSCs devices.[13] This is because the good conductivity of carbon-based materials and the synergistic effect of TiO_2 photoelectric properties can effectively promote electron transport and inhibit electronic recombination. Moreover, carbon materials acting on the photoanode may have a certain positive effect on the improvement of dye absorption and catalytic photoelectric activity.[14,15] Inspired by the above

[a]*School of Resources, Environment and Materials, Guangxi University, Nanning, 530004, China. E-mail: hdy@gxu.edu.cn; hdygxu@163.com; wxxxljj@163.com; Tel: +86-771-3232200*

[b]*State Key Laboratory of Featured Metal Materials and Life-cycle Safety for Composite Structures, Guangxi University, Nanning, 530004, China. E-mail: Qinxiang542968@163.com; 785631176@qq.com; 1319548675@qq.com*

† Electronic supplementary information (ESI) available. See DOI: https://doi.org/10.1039/d3ra00545c

‡ These authors contributed equally to this work.

advantages, we mixed non-carbonized materials (such as chlorophyll and anthocyanins natural dyes) with TiO_2 before doping and then calcined the mixture to form carbon materials naturally dispersed in TiO_2. The abundant functional groups of anthocyanins, particularly hydroxyl and carboxyl groups can interact with the Ti–O bond on TiO_2 molecules to form colored TiO_2. The functional groups were adsorbed on TiO_2 at high-temperature to form carbon materials and were evenly dispersed in TiO_2. Compared with the traditional mechanical method of doping carbon materials into TiO_2, the use of molecular bond adsorption could make the carbon materials disperse more evenly in TiO_2, thereby reducing the obstruction of the electron shuttle and further increasing electron migration.

The commonly used CE is the rare and precious metal Pt, which is costly and harmful to the environment, and severely restricts the development and application of DSSCs.[16] For this reason, research work on carbonaceous materials,[17,18] transition metal compounds[19] and intrinsic conducting polymers[20] as alternatives to Pt has received attention. Among them, carbon-based materials have the advantages of low cost, strong electron transport ability, and corrosion resistance in electrolytes. However, the contact between carbon-based materials and the transparent conductive substrate is unstable, which seriously affects the electrocatalytic ability of the electrode. In addition, metal compounds are prone to corrosion when in contact with electrolytes, which limits their direct application.[21] Yun *et al.* combined bio-based carbon (BC) with transition metal compounds (TMCs) for counter electrodes, and its PCE was about 15% and 74% higher than that of BC CE and TMC CE.[22] Qureshi *et al.* synthesized a hybrid GO/Fe_3O_4 nanocomposite, which was also used as the counter electrode of DSSCs, and its PCE was 57% of Pt CE.[23] Hence, the combination of carbon materials and metal compounds is an effective and direct means to improve the electrocatalytic properties of carbon-based materials and apply them as DSSCs. Compared with Pt, Ni, and Pt share similar valence electron configurations and adjacent positions, which are expected to be low-cost analogs of Pt. Wang *et al.* prepared $NiCo_2S_4$ nanoparticles loaded on carbon nanofibers (CNFs), benefitting from the tubular structure of CNFs, nickel and cobalt ions were loaded on the surface of CNFs to exhibit high conductivity.[24] Based on these, we used the residue after extracting the pigment from blueberries to prepare N-doped blueberry-derived porous carbon-loaded Ni nanoparticles (Ni@NPC-*X*) for use in DSSC counter electrodes.

Herein, we have creatively designed two functional electrode materials (photoanode, counter electrode) with blueberries as the key performance improvement, and verified the contribution of blueberries to the DSSC electrode. The P25/PBP photoanode was prepared by mixing TiO_2 (P25) and the blueberry dye, while the Ni@NPC-*X* counter electrode was prepared by loading Ni nanoparticles onto biomass blueberry-based N-doped carbon material. The elemental composition, structural composition, surface morphology, and photovoltaic parameters were analyzed by XRD, Raman spectroscopy, XPS, SEM, and *J*–*V* curves. The electrochemical characteristics of the Ni@NPC-*X* material in the supercapacitor electrodes were used to further confirm their excellent electrocatalytic performance and energy storage capacity. This research provided new ideas for blueberry-based photovoltaic-electric energy systems.

2 Experimental sections

2.1 Materials and reagents

Nickel acetate tetrahydrate ($Ni(CH_3COO)_2 \cdot 4H_2O$), chloroplatinic acid hexahydrate ($H_2PtCl_6 \cdot 6H_2O$), Ru-based photosensitizer dye (N719) were provided by Aladdin Chemical Reagent Co., Ltd (Shanghai, China). Polymer spacers (Surlyn) with a thickness of 60 μm and FTO glass slides with a size of 2.5 × 2 cm (resistivity of ~7 ohm sq^{-1}) were provided by Yingkou Opivite New Energy Technology Co., Ltd (Yingkou, Liaoning, China). Fresh blueberries (produced in Peru) were obtained from Beijing Jingdong Century Trading Co., Ltd (Beijing, China).

2.2 Preparation of electrode materials

2.2.1 Preparation of the P25/PBP composite. 1 g of blueberry powder (BP) was dissolved in 30 ml of ethanol to extract the blueberry dye (anthocyanins) to obtain a purified and dissolved blueberry dye solution. The above solution was dried at 50 °C for 12 h and ground into powder (PBP). 1.2 g TiO_2 (P25) and 0.05 g PBP were mixed with an appropriate amount of ethanol to obtain a TiO_2-blueberry dye composite (P25/PBP). To obtain P25/PBP with different PBP contents, the added amount of PBP was 0.025 g, 0.1 g, and 0.2 g, respectively, denoted as P25/PBP-1, P25/PBP-2, and P25/PBP-3, respectively.

The preparation strategy of the Ni@NPC-*X* composite is represented in Fig. S1.† Blueberry powder (BP) was pre-carbonized in nitrogen at 700 °C for 2 h to obtain a pre-carbonized BP. 1 g of pre-carbonized BP was added to 20 ml of 2 g KOH solution and homogenized by stirring at 25 °C for 4 h. The mixed solution was concentrated at 70 °C for 24 h, then annealed at 700 °C for 2 h in nitrogen, and after the temperature dropped to 25 °C, the resulting sample was stirred in 1 M HCl for 2 h. The samples were then purified with distilled water and ethanol until the cleaning solution was neutral, and dried at 80 °C to obtain PC. 1 g of PC, 0.5 g of $Ni(CH_3COO)_2 \cdot 4H_2O$, and 1 g of melamine (1.5 g or 2 g) were added into 60 ml distilled water, hydrothermal heating at 160 °C for 12 h, and then annealing at 600 °C for 3 h under N_2 atmosphere. Finally, the N-doped porous carbon composites loaded with Ni nanoparticles were obtained and named Ni@NPC-*X* ($X = 1$, 1.5, and 2, representing the amount of melamine added). In addition, in order to compare the effect of N-doping, Ni@PC was prepared by the same method, except that melamine was not added.

2.3 Assembling of DSSCs

2.3.1 The preparation of photoanodes. FTO conductive glass was washed twice with detergent, conductive glass cleaning solution, and distilled water in a sequence, and dried in an oven. Firstly, the P25/PBP sol was evenly scraped on the clean FTO glass by the scraper technique to obtain the P25/PBP electrode by sintering at 450 °C for 30 min. The upper P25/

PBP electrode was then kept in a 40 mM $TiCl_4$ solution at 70 °C for 30 min and re-sintered at 450 °C for 30 min. Finally, the prepared P25/PBP electrode was immersed in 0.5 mM N719 dye at 25 °C for 18 h in dark to obtain a dye-sensitized photoanode.

2.3.2 Preparation of counter electrodes (CEs). 0.2 g of the prepared Ni@NPC-*X*, 15 mg of TiO_2, and 20 μL of Triton X-100 were placed in 1 ml of distilled water to obtain the mixed slurry by ultrasonication for 1 h. The mixed slurry was evenly scraped on the clean FTO glass by the scraper technique to obtain Ni@NPC-*X* CEs by sintering at 450 °C for 30 min under N_2 atmosphere. Pt CE was obtained by adding 20 mM $H_2PtCl_6 \cdot 6H_2O$ onto FTO glass as a control and sintering at 450 °C for 30 min.

2.3.3 The assembly of DSSCs. The dye-adsorbed photoanode (P25/PBP, P25) and counter electrode (Ni@NPC-*X*, Pt) were assembled with a 60 μm Surlyn film to obtain the DSSCs. Then, an electrolyte consisting of 0.025 M I_2, 0.1 M guanidine thiocyanate, 0.5 M 4-*tert*-butylpyridine, 0.6 M 1-methyl-3-propylimidazolium iodide in a mixture of acetonitrile/valeronitrile (85 : 15 v%) was filled into the through hole of the CE cell, and then the hole was sealed with a sealing film.

2.4 Characterization and performance tests

The physical/chemical structures of the DSSCs electrodes were characterized using an X-ray diffractometer (XRD), scanning electron microscope (FE-SEM), X-ray photoelectron spectroscopy (XPS), Fourier transform infrared spectrometer (FTIR), Raman spectrometer, and Brunau–Emmett–Taylor (BET), as detailed in the ESI.† DSSCs performance tests included photocurrent density voltage (*J–V*) curves, electrochemical impedance spectroscopy, Tafel polarization, cyclic voltammetry, and open circuit voltage decay (OCVD) curves, as detailed in the ESI.†

3 Results and discussion

3.1 Morphology and composition analysis

In order to explore the effect of PBP doping on the morphology of P25 particles, P25 and P25/PBP were characterized by SEM. The surface of the P25 photoanode hints at the homogeneity of the TiO_2 particle distribution (Fig. 1a–c). After adding PBP, the particle size of TiO_2 in P25/PBP (Fig. 1e and f) increases, and the interparticle gap becomes larger, which can enable better adsorption of the N719 dye. Further, as shown in Fig. S2,† the addition of PBP increased the S_{BET} of P25/PBP (36.89 $m^2\ g^{-1}$) compared with P25 (24.59 $m^2\ g^{-1}$), which is conducive to increasing the dye loading capacity of N719.

For CEs, it can be clearly seen that the blueberry powder-based carbon (PC) displayed a porous structure (Fig. 2a–c) originating from KOH-activated etching. In Ni@PC that is not doped with N, the Ni nanoparticles were loaded on the surface of PC, and the pore structure may have been covered, causing the diffusion of the electrolyte through the material to be hindered (Fig. 2d–f). Notably, when N was doped into the Ni@PC, the base morphology of the Ni@PC changed from a flat surface to a 3D petal-like shape (Fig. 2g–i). This promoted the diffusion of the electrolyte through the material, and the characteristic shape facilitated the loading of Ni nanoparticles. As shown in Fig. 2i, there were no other impurities on the surface of the Ni@NPC-1.5 composite material. Its morphology presented an open petal-like shape, and the size of the Ni particles loaded was ~10 nm. Furthermore, the SEM mapping shown in Fig. 2j revealed the uniform elemental distribution of C, N, and Ni in the entire Ni@NPC-1.5, suggesting the uniformity of Ni nanoparticles on N-doped PC from the aspect of morphology distribution.

Further to understand the influence of N doping on the morphology of Ni@NPC-*X*, morphologies at different N doping levels were studied, as shown in Fig. S3.† The structural characteristics of the Ni@NPC-1.5 composite material showed that the morphology of the composite material can be adjusted by reasonably controlling the N-doped content. The pore characteristics of PC, Ni@PC, Ni@NPC-1, Ni@NPC-1.5, and Ni@NPC-2 are represented in Fig. S4.† Carbon-based materials exhibited a large specific surface area (S_{BET}), which enhanced the number of active sites and electrolyte contact, and thus reflecting as prospective to improve the electrochemical performance of CE.

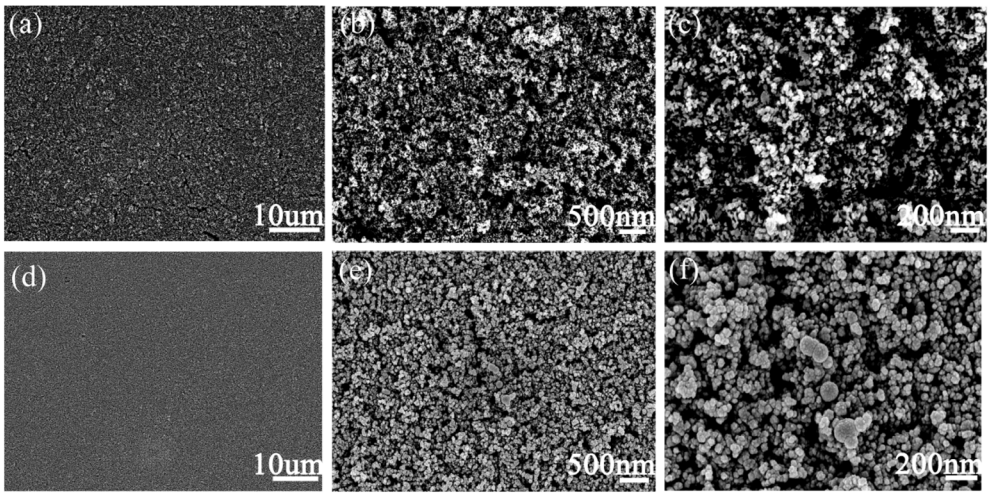

Fig. 1 SEM images of P25 (a–c) and P25/PBP (d–f).

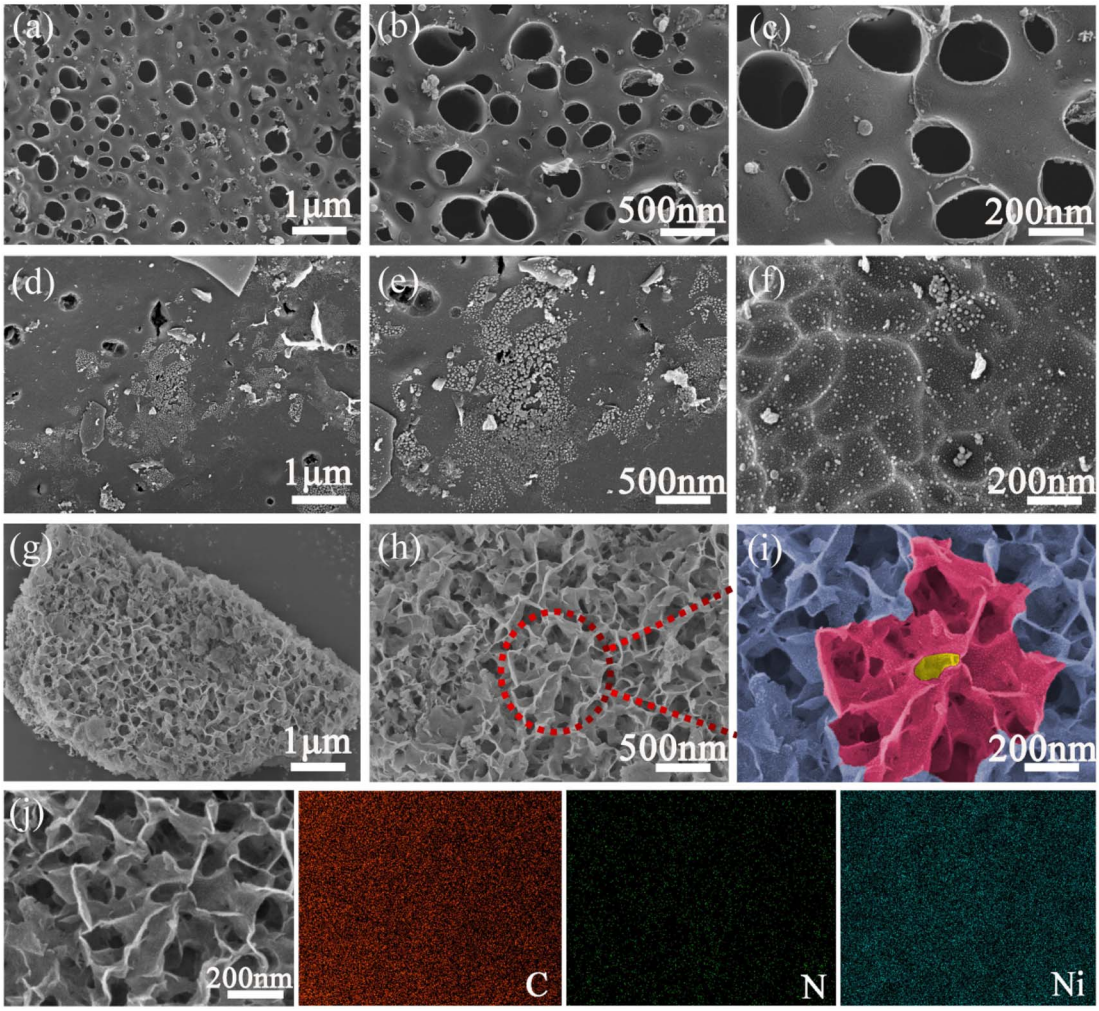

Fig. 2 SEM images of PC (a–c), Ni@PC (d–f), Ni@NPC-1.5 (g–i), and SEM mapping (j) of Ni@NPC-1.5.

PBP and P25 were bonded through functional groups to form a colored P25 powder. The crystal structure and composition of PBP, P25, and P25/PBP after calcination at 450 °C were analyzed by XRD and Raman spectroscopy (Fig. 3a). For P25, the diffraction peaks at $2\theta = 25.27°$, 37.01°, 37.70°, 38.49°, 48.11°, 53.90°, 55.11°, 62.08°, 62.71°, 68.69°, 70.30°, 74.02°, and 75.06° corresponded to the (101), (103), (004), (112), (200), (105), (211), (213), (204), (116), (220), (107), and (215) crystal planes of anatase.[25] The diffraction peaks at $2\theta = 27.40°$, 36.11°, 39.18°, 41.19°, 44.10°, and 54.29° corresponded to (110), (101), (200), (111), (210), and (211) crystal planes of rutile.[26] The diffraction peak at $2\theta = 23°$ was attributed to the (002) crystal plane of amorphous carbon, suggesting that PBP was constructed by sintering at 450 °C is an impurity-free carbon, which was also verified from the FTIR analysis (Fig. S5a†).[27] P25 and P25/PBP showed little difference in diffraction peaks, suggesting that PBP did not have a negative effect on P25 from the lattice structure level. The Raman spectroscopy analysis of PBP, P25, and P25/PBP, shown in Fig. 3b, also confirmed the same analysis results. The appearance of anatase titanium dioxide located at 143, 397, 515, and 639 cm^{-1}, and the D and G peaks of the graphite at 1365 and 1590 cm^{-1} in P25 suggested the existence of P25 and C atoms in the P25/PBP composite.[25]

The crystal characteristics of the nitrogen-doped porous carbon-supported Ni composites (Ni@NPC-*X*) were investigated using XRD and Raman spectroscopy (Fig. 3c and d). The (002) and (100) planes of the typical graphitic carbon were found in all samples near $2\theta = 23°$ and 43.5°, implying the main features of amorphous carbon.[27] Compared with PC and Ni@PC without N doping, the diffraction peak of Ni@NPC-*X* on the (002) crystal plane was shifted, and the shift amplitude increased with the increase in the melamine proportion, which may be due to the double effect of KOH and melamine leading to more defects in the carbon-based material.[28] In addition, the (111), (200), and (220) planes of Ni were also found at $2\theta = 44.3°$, 51.6°, and 76.2°, respectively.[29] In Fig. 3d, the distinct peaks at ~1351 cm^{-1} and ~1589 cm^{-1} were considered to be typical D and G peaks of graphite.[30] Furthermore, I_D/I_G of Ni@NPC-1.5 (0.99) was stronger than that of Ni@NPC-1 (0.94), and Ni@NPC-2 (0.96), indicating that the structure of Ni@NPC-1.5 had many structural defects, which resulted in the increase of electrochemically active sites and the beneficial effect of the electrolyte transport.[31]

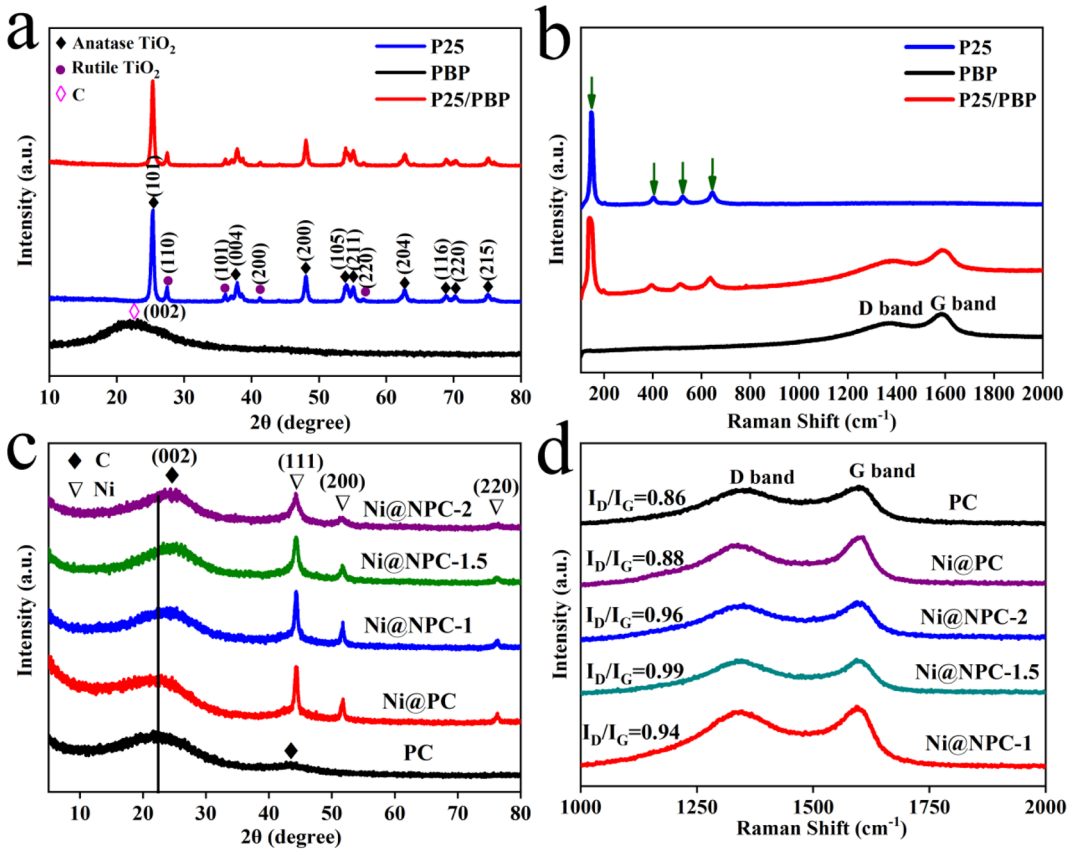

Fig. 3 XRD patterns (a and c) and Raman spectra (b and d).

Furthermore, Fig. 4 shows the chemical composition, chemical bond properties, and bonding states of the surface elements on P25/PBP and Ni@NPC-1.5 surfaces. For P25/PBP (Fig. 4a), the presence of Ti, O, and C is supported. The high-resolution Ti 2p spectrum showed representative strong binding energy peaks at 458.4 eV and 464.1 eV ascribed to Ti $2p_{3/2}$ and Ti $2p_{1/2}$, respectively.[32] The deconvolution of the high-resolution O 1s spectrum indicated peaks at 529.7 eV and 530.6 eV, due to Ti–O and OH on the Ni@NPC-1.5 surface (Fig. 4e). The high-resolution spectrum of C 1s indicated peaks at 284.4 eV, 285.6 eV, and 288.3 eV corresponding to C–C, C–O, and C=O, respectively.[33,34]

In particular, the full spectrum Ni@NPC-1.5 shown in Fig. 4c indicated the presence of C, N, and Ni elements, which confirmed that N was doped into the sample. The formation of N-doped PC was further illustrated by the presence of C–N and C=N bonds indicated by the peaks at 285.8 eV and 286.7 eV in the high-resolution C 1s spectrum in Fig. 4g.[35] Analysis of the N 1s spectrum revealed that the proportions of pyridine N, pyrrolic N, and graphitic N at 398.5, 400.5, and 402.9 eV were 8.4, 51, and 40.6%, respectively.[36] The high proportion of pyridine N and pyrrole N formed in the carbon structure has the potential for electrocatalysis.[37] Graphite N can improve the electrical conductivity of carbon materials, and both can play a vital role in improving the catalytic reduction performance of carbon materials.[38] Moreover, as shown in Fig. 4i, the characteristic peak at 854.8 eV for the high-resolution Ni 2p belongs to metallic Ni, which provides the basis for that $Ni(CH_3COO)_2 \cdot 4H_2O$ was carbo-thermally reduced to Ni monomers.[39] The trace Ni^{2+} with the characteristic peak at 860.9 eV may be caused by the surface oxidation in the air.

3.2 Performance of DSSCs assembled using P25/PBP and Pt

The fabricated DSSCs of P25-Pt, P25/PBP-Pt, P25/PBP-1-Pt, P25/PBP-2-Pt, and P25/PBP-3-Pt were tested under 1 sun condition with 0.25 cm^2. As shown in Table 1 and Fig. 5, the analysis results of the *J–V* curve showed that the descending order of PCE was P25/PBP-Pt (5.82%) > P25/PBP-2-Pt (5.63%) > P25/PBP-1-Pt (5.46%) > P25-Pt (4.96%) > P25/PBP-3-Pt (4.11%) (Fig. 5a). P25/PBP-Pt showed the highest PCE, which is better than pure P25-Pt. The open circuit voltage (V_{oc}) was 0.71 V for both P25/PBP-Pt and P25-Pt, and the fill factor (FF) increased with the addition of PBP, possibly due to the better conductivity of carbon materials.[40] The J_{sc} of P25/PBP-Pt (14.66 mA cm^{-2}) was 13.3% higher than that of P25-Pt (12.94 mA cm^{-2}), which enhanced the performance of P25/PBP-Pt. The addition of PBP played a positive role in the enhancement of photocurrent, which was also reflected in PCE. The addition of PBP increased the optical absorbance of P25/PBP in the visible region (supported by Fig. S5b†). The Nyquist plots (Fig. 5b) and Bode plots (Fig. 5c) of DSSCs fabricated at different contents of PBP, and *J–V* curves (Fig. 5d) of P25-Pt and P25/PBP-Pt further confirmed the effect of PBP on the PCE enhancement.

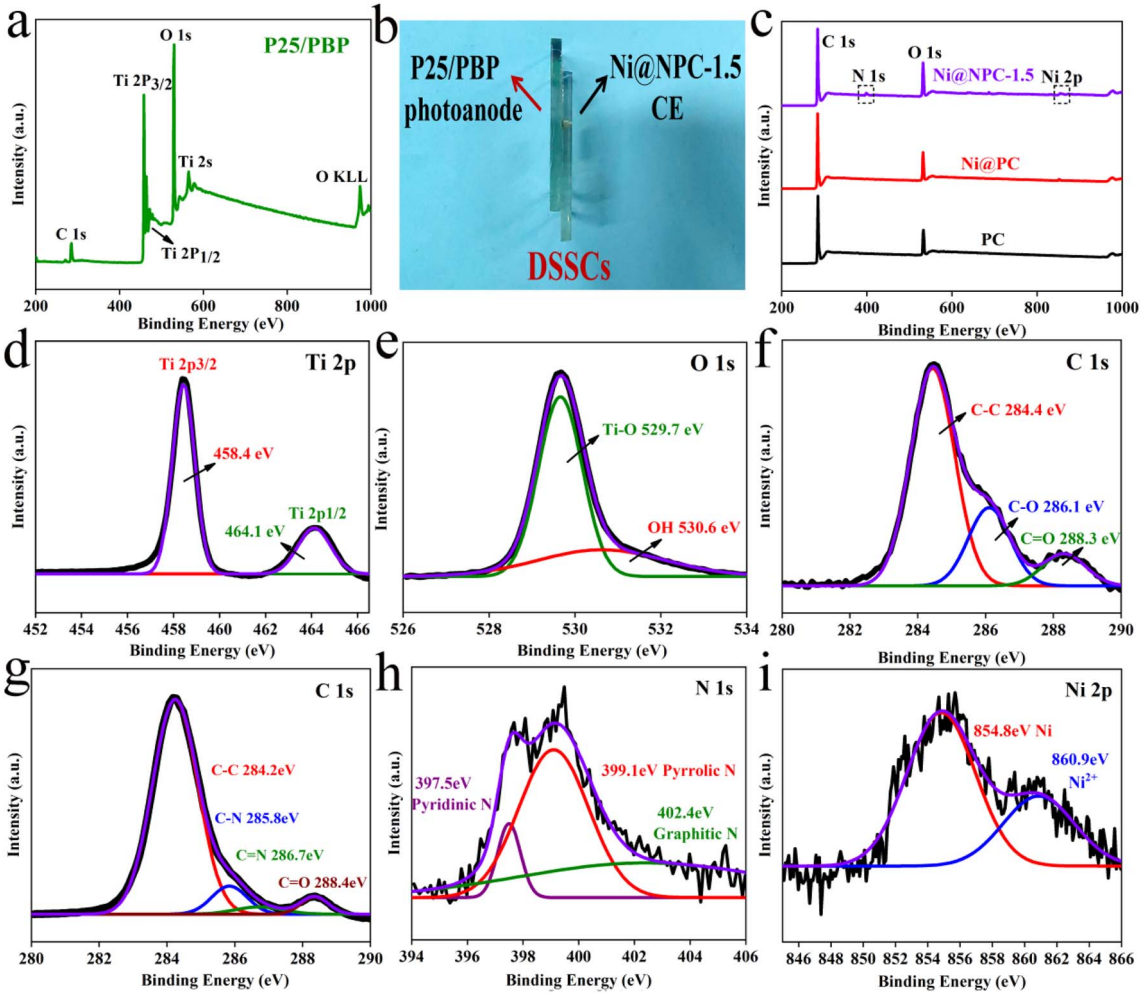

Fig. 4 XPS spectra of P25/PBP, Ni@PC, PC and Ni@NPC-1.5 (a–i).

Table 1 Performances of P25-Pt and P25/PBP-Pt[a]

DSSCs	V_{oc} (V)	J_{sc} (mA cm^{-2})	FF	PCE (%)	R_s (Ω)	R_{ct} (Ω)	f_{max} (Hz)
P25-Pt	0.71 ± 0.01	12.94 ± 0.2	0.54 ± 0.01	4.96 ± 0.08	23.1	83.9	12.10
P25/PBP-Pt	0.71 ± 0.01	14.66 ± 0.1	0.56 ± 0.01	5.82 ± 0.08	21.6	76.8	5.63
P25/PBP-1-Pt	0.71 ± 0.01	12.62 ± 0.2	0.61 ± 0.01	5.46 ± 0.02	21.0	86.9	8.06
P25/PBP-2-Pt	0.67 ± 0.01	13.56 ± 0.2	0.62 ± 0.01	5.63 ± 0.06	23.5	78.7	6.62
P25/PBP-3-Pt	0.72 ± 0.01	8.38 ± 0.3	0.68 ± 0.01	4.11 ± 0.08	23.7	100.7	8.46

[a] V_{oc}: open-circuit voltage, J_{sc}: short-circuit current density, FF: fill factor, PCE: power conversion efficiency, R_s: volume resistance, R_{ct}: charge-transfer resistance.

EIS-curve analysis was adopted as a more comprehensive understanding of the relationship and underlying reasons between the introduction of PBP and the enhancement of opto-electronic properties (Fig. 5e). R_s and R_1 between the electrolyte/CE interfaces of P25/PBP-Pt and P25-Pt were approximately the same,[41] due to the use of Pt CEs. The main difference is that the R_{ct} between the TiO_2/dye/electrolyte interfaces (76.8 Ω) of P25/PBP-Pt was less than P25-Pt (83.9 Ω), which meant that P25/PBP-Pt had better electron transfer ability.[42] This is beneficial to substantially increase the PCE of DSSCs.

Fig. 5f depicts the Bode plots of P25/PBP-Pt and P25-Pt. Compared with ~12.1 Hz for P25-PT, the f_{max} value for P25/PP-PT had a beneficial decrease (~5.63 Hz). According to the electronic lifetime calculation formula: $\tau_n = 1/2\pi f_{max}$,[43] it can be seen that P25/PBP-Pt had a larger τ_n and a faster electron transfer ability. This result indicates that the addition of PBP has a positive effect on accelerating the electron transfer ability of the P25 photoanode.

Dark current and OCVD tests and analyses are necessary to study the effect of adding PBP on the electron lifetime. Fig. 5g

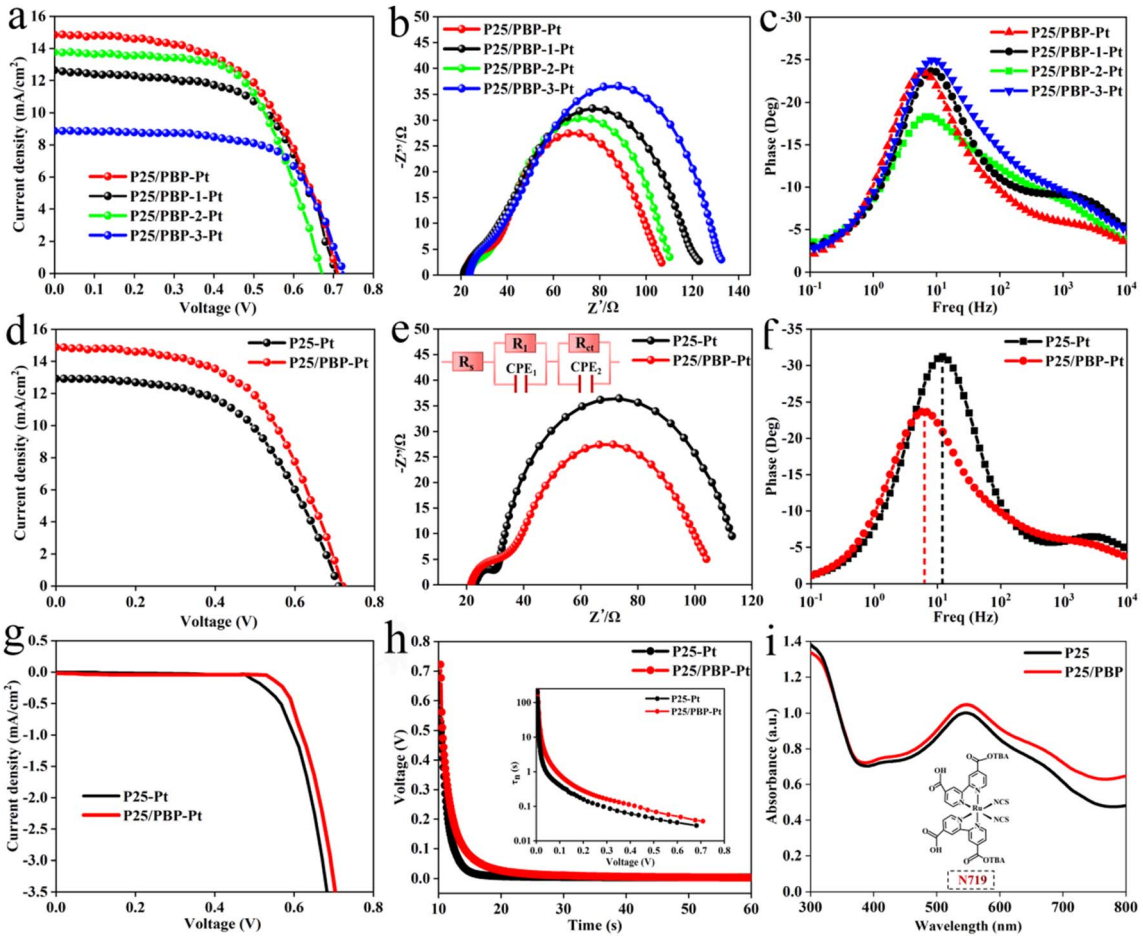

Fig. 5 *J*–*V* curves (a), Nyquist plots (b), and Bode plots (c) of DSSCs assembled with different contents of PBP; *J*–*V* curves (d), Nyquist plots (e), Bode plots (f), dark current diagrams (g), *V*–*T* curves (h), UV-vis absorption spectra (i) of P25/PBP and P25.

shows the *J*–*V* curve of P25/PBP-Pt and P25-Pt under dark condition. Under the additional voltage, P25/PBP-Pt showed a lower dark current, indicating that the dark reaction and the hole–electron recombination of P25/PBP-Pt were small. As can be seen from the OCVD curve in Fig. 5h, the voltage decay rate of P25/PBP-Pt was slower while the light source was removed. As shown in the τ_n–*V* curves in the inset of Fig. 5h, in the voltage range of 0–0.7 V, the τ_n of the P25/PBP-Pt is greater than that of P25-Pt.[44]

Furthermore, as shown in Fig. 5i, the UV-vis absorptions of the photoanode after the dye adsorption on P25/PBP and P25 with similar thickness were tested. Both P25/PBP and P25 showed strong absorption peaks at 550 nm in the visible region of 300–800 nm, corresponding to the main absorption peak of N719 dye. The absorbance of P25/PBP at the maximum absorption peak was 6.8% higher than that of P25. This result showed that the addition of PBP enhanced the absorption capacity of P25/PBP to N719 dye, thereby, increasing J_{sc}. Using 0.5 M NaOH to analyze the content of N719 dye loaded on the photoanode, the loading of the P25/PBP (15.3×10^{-8} mol cm^{-2}) was greater than that of P25 (16.8×10^{-8} mol cm^{-2}).

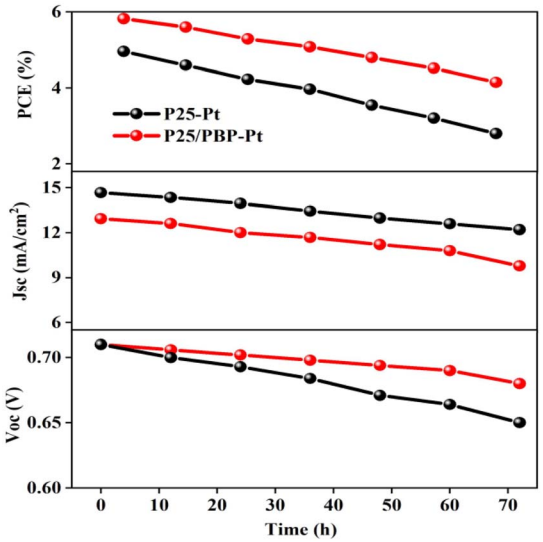

Fig. 6 The electrochemical stability of DSSCs based on P25 and P25/PBP photoanode.

The electrochemical stability of DSSCs assembled with P25/PBP photoanode and Pt CE was measured under simulated illumination in the I^-/I_3^- electrolyte for 72 h against the P25 photoanode. As shown in Fig. 6, the V_{oc} and J_{sc} of the DSSCs based on the P25 photoanode continued to decrease after the test, resulting in a decrease in the PCE value from the initial value of 4.96% to 2.8%, and the decay rate reached 43.5%. For DSSCs assembled with the P25/PBP photoanode, V_{oc} decreased from 0.71 V to 0.68 V, J_{sc} decreased from 14.66 mA cm^{-2} to 12.21 mA cm^{-2}, and the PCE decay rate was only 28.7% with the initial value of 5.82%; the decay rate of P25/PBP photoanode was lower than that of the P25 photoanode. PBP not only increased the adsorption of dyes on the photoanode but also effectively inhibited the decay of DSSCs to a certain extent, providing a sustainable and stable capacity.

3.3 Performance of DSSCs assembled by P25/PBP and Ni@NPC-*X*

Nitrogen-doped porous carbon-covered Ni composites (Ni@NPC) were strategically prepared by using the natural three-dimensional network structure of biomass-based carbon as a carrier and introducing Ni nanoparticles to reduce the agglomeration of metal particles. Therefore, the comprehensive performance of the DSSCs assembled with Ni@NPC as the counter electrode and P25/PBP as the photoanode was evaluated.

Fig. 7a shows the *J*–*V* curves of the DSSCs assembled with P25/PBP and Ni@NPC-*X*. Fig. 7b shows the schematic of the assembled DSSCs of the P25/PBP photoanode and Ni@NPC-*X* CEs. The relevant PV evaluation indexes are represented in Tables 2 and S1.† The PCE of Ni@PC-based DSSCs (2.94%) is greater than that of PC-based DSSCs (1.86%), reflecting the

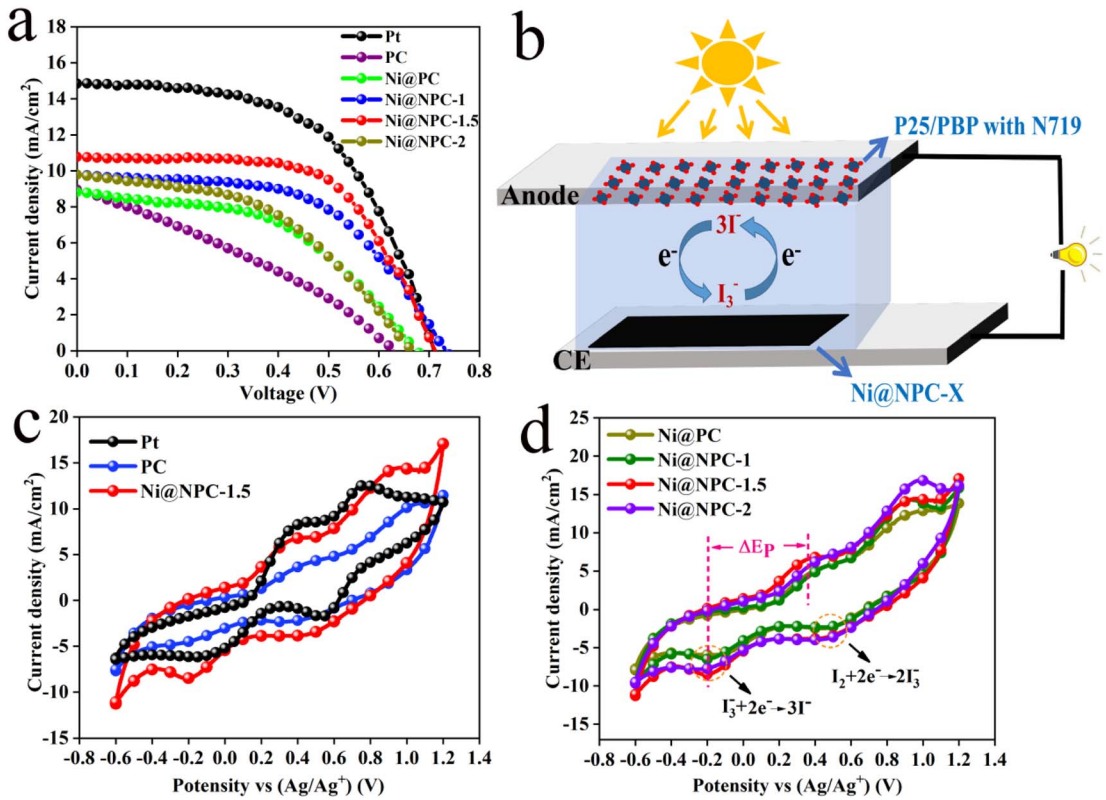

Fig. 7 *J*–*V* curves (a), schematic of the assembled DSSCs of P25/PBP photoanode and Ni@NPC-*X* CEs (b), *CV* curves (c and d) of Ni@PC, Ni@NPC-*X*, Pt, and PC at 50 mV s^{-1}.

Table 2 Photovoltaic and electrochemical parameters of the cells with different CEs[a]

CEs	V_{ov} (V)	J_{sc} (mA cm^{-2})	FF	PCE (%)	E_p (mV)	I_p (mA cm^{-2})	R_{ct} (Ω)	R_{s1} (Ω)
PC	0.63 ± 0.01	8.93 ± 0.2	0.33 ± 0.01	1.86 ± 0.02	882	−4.83	13.61	20.67
Ni@PC	0.68 ± 0.01	8.49 ± 0.4	0.51 ± 0.02	2.94 ± 0.04	742	−6.02	9.82	22.96
Ni@NPC-1	0.72 ± 0.01	9.49 ± 0.2	0.55 ± 0.01	3.88 ± 0.05	682	−6.50	5.39	16.67
Ni@NPC-1.5	0.70 ± 0.01	11.17 ± 0.4	0.62 ± 0.02	4.86 ± 0.08	628	−8.50	3.02	20.09
Ni@NPC-2	0.67 ± 0.01	9.13 ± 0.5	0.49 ± 0.02	2.99 ± 0.05	721	−7.83	7.08	17.53
Pt	0.71 ± 0.01	14.66 ± 0.1	0.56 ± 0.01	5.82 ± 0.08	588	−6.15	4.91	17.29

[a] I_p: current density of cathode peak, E_p: difference of REDOX peaks, R_{ct}: charge transfer resistance, R_{s1}: series resistance.

enhanced catalytic reduction ability of PC for I_3^- after Ni addition. In addition, DSSCs based on N-doped Ni@NPC-*X* CEs have significantly improved the photovoltaic performance compared to that showed by PC and Ni@PC, and showed an enhanced effect in the catalytic reduction of I_3^-. With the increase in the N doping content, the FF values from Ni@NPC-1 to Ni@NPC-1.5 gradually increased, and the increase in the FF value promoted the improvement in the PCE values. The addition of excessive melamine reduces the S_{BET}, resulting in the reduction of the surface contact between the electrolyte and electrode and the increase of the internal resistance of the electron transmission, which is reflected in the decrease of FF value at Ni@NPC-2. Correspondingly, the PCE of Ni@NPC-*X* (*X* = 0, 1, and 1.5) CEs has a certain relationship with the amount of N doping, which changes from an increasing trend to decreasing trend, that is, when the N doping amount reaches 2 g, the PCE decreased. Only when the amount of N doping is appropriate, the PCE of Ni@NPC-1.5 is the highest, reaching 4.86%, with V_{oc} of 0.70 V, J_{sc} of 11.17 mA cm^{-2}, and FF of 0.62.

The electrocatalytic activity and I_3^- reduction reversibility of PC, Ni@NPC-*X*, and Pt CEs were studied from *CV* curves, and the photovoltaic performance differences of different CEs-based DSSCs were evaluated.[45] The *CV* curves of CEs at 50 mV s^{-1} are illustrated in Fig. 7c and d. Notably, Ni@NPC-*X* has a much larger background current density than PC, Ni@PC, and Pt due to the increase of vacancy defects in the N-doped composites and the effective adsorption of I_3^- ions at the defect sites, which is beneficial for the generation of double capacitance.[46] It can be seen that in all composite materials CEs, the I_p values vary from high to low, following I_p(Ni@NPC-1.5: 8.5 mA cm^{-2}) > I_p(Ni@NPC-2: 7.83 mA cm^{-2}) > I_p(Ni@NPC-1: 6.5 mA cm^{-2}) > I_p(Ni@PC: 6.02 mA cm^{-2}) > I_p(PC: 4.83 mA cm^{-2}), which is the basis for the highest electrocatalytic activity of Ni@NPC-1.5.[47] The order of ΔE_p values varying from low to high is ΔE_p(Ni@NPC-1.5: 628 mV) < ΔE_p(Ni@NPC-1: 682 mV) < ΔE_p(Ni@NPC-2: 721 mV) < ΔE_p(Ni@PC: 742 mV) < ΔE_p(PC: 882 mV), showing that the increase of reaction power speed leads to the decrease of ΔE_p value.[48] The higher I_p and smaller ΔE_p value of Ni@NPC-1.5 comprehensively reflect its superiority in catalytic reduction of I_3^-. The reason may lie in the enhancement of the specific surface area of the vacancy defect sites and carbon-based materials by N doping, promoting the adsorption of electrolytes and accelerating the transfer of charge, which are beneficial to the realization of high electrocatalysis during the catalytic reduction of I_3^- and fast reaction kinetics.

Analysis of the Nyquist plots of symmetric cells assembled based on the same CE is essential to further explain the difference in key properties of DSSCs constructed from different CEs (Fig. 8a and 9).[49] The schematic diagram of the symmetrical cell assembled based on Ni@NPC-*X* CE is shown in Fig. 8b. In fact, the R_{s1} value of all CEs is close to that of Pt, concentrated between 16–23 Ω, indicating that the prepared CEs material has good adhesion to conductive glass. Notably, Ni@NPC-*X* exhibited a low R_{ct} of 3–8 Ω, in contrast to PC (13.61 Ω) and Ni@PC (9.82 Ω), which also implied that N doping enhanced the well-being of I_3^- reduction through good electrocatalytic activity. As shown in Fig. 8d, the excellent electrocatalytic performance of the three-dimensional network structure of

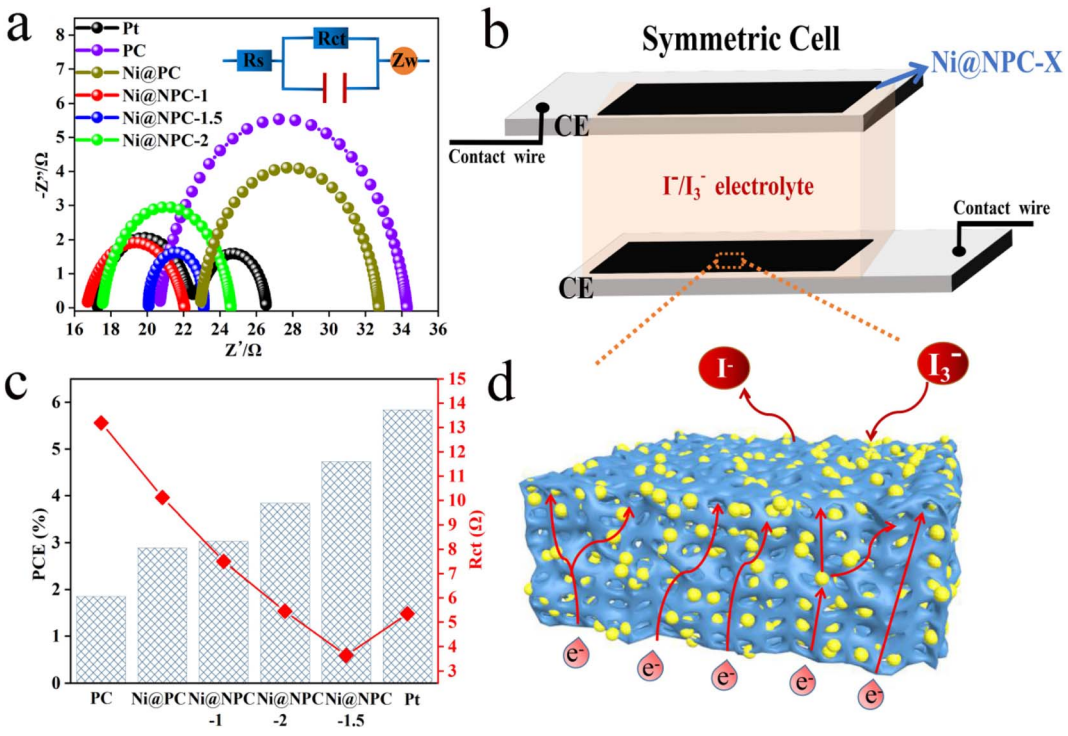

Fig. 8 Nyquist plots (a) of PC, Ni@PC, Ni@NPC-*X*, and Pt under a bias voltage of 0 V based on the symmetrical cells, Schematic diagram of a symmetrical cell assembled based on Ni@NPC-*X* CE (b), PCE and R_{ct} values (c), schematic of Ni@NPC-*X* CE reduction I_3^- (d).

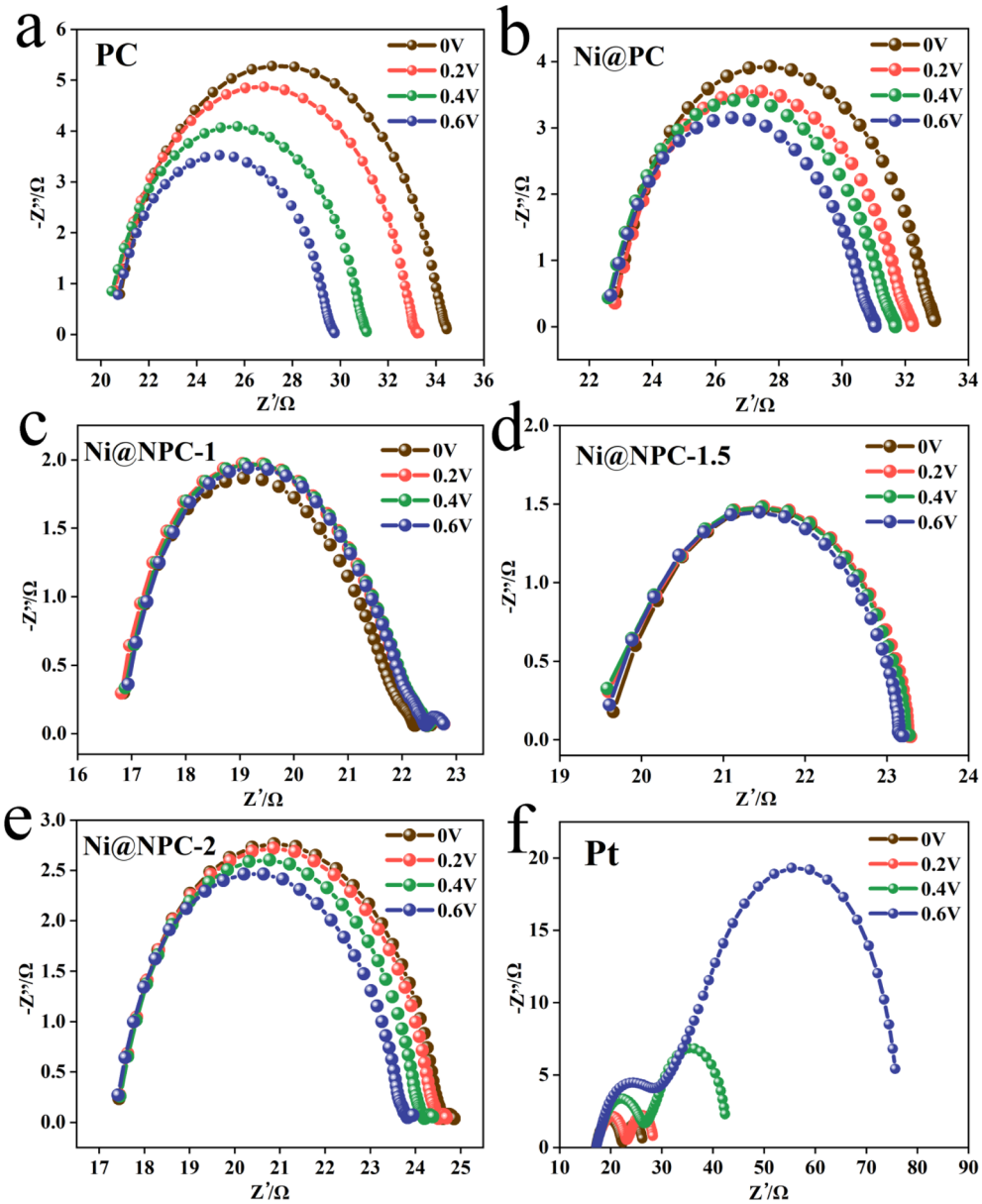

Fig. 9 Nyquist plots at various bias voltages.

multiple defect sites provided by the N-doped biochar cooperates with Ni metal ions. Therefore, the proper N-doped Ni@NPC-1.5 has the lowest R_{ct} of 3.02 Ω, which is even lower than that of Pt (4.91 Ω). Ni@NPC-1.5 with low R_{ct} has a higher PCE that is closer to that of Pt, which corresponds to the R_{ct} and PCE curves shown in Fig. 8c.

Table 3 PCE values of DSSCs based on various biomass-derived carbon CE

Biomass carbon CE	V_{oc} (V)	J_{sc} (mA cm^{-2})	FF	PCE (%)	PCE (Pt) (%)	S_{BET} (m^2 g^{-1})
Aloe peel[51]	0.68	13.25	0.58	5.20	6.46	—
Pomelo peel[52]	0.67	13.40	0.53	4.45	6.71	534.45
Chitin[53]	0.69	11.33	0.61	4.81	6.30	359.7
Poplar[54]	0.62	12.15	0.24	1.89	6.23	272.8
Rice husk[55]	0.67	13.97	0.59	5.54	6.32	268.7
Bagasse[56]	0.69	10.70	0.37	2.48	6.08	—
Waste carton[57]	0.65	11.69	0.60	6.19	7.51	655.36
Blueberry (this work)	0.70	10.77	0.63	4.86	5.84	1185.7

Fig. S7† represents the Tafel polarization curves of symmetric cells assembled by the various CEs, which are mainly adopted to explain the relationship between the overpotential voltage (V) and the logarithmic current density (log J). The exchange current density (J_0) (0.002 mA cm^{-2}) of the Ni@NPC-1.5 composite was greater than that of PC (0.00093 mA cm^{-2}), Ni@PC (0.001 mA cm^{-2}), Ni@NPC-1 (0.0014 mA cm^{-2}) and Ni@NPC-2 (0.00128 mA cm^{-2}) and Pt (0.0015 mA cm^{-2}), indicating that Ni@NPC-1.5 has good electrocatalysis on I_3^- reduction.[50] According to eqn (1), the result of the J_o value is also consistent with the changing trend of R_{ct} in the Nyquist plots.

$$J_0 = \frac{RT}{nFR_{ct}} \quad (1)$$

In addition, the limiting diffusion current density (J_{lim}) value of the Ni@NPC-1.5 composite material is also greater than that of other CE materials. According to eqn (2), it can be confirmed that the surface between the I_3^- ion in the electrolyte and Ni@NPC-1.5 has a larger diffusion coefficient (D).

$$J_{lim} = \frac{2neDCN_A}{l} \quad (2)$$

The strong diffusion coefficient of the as-prepared composite CEs is mainly due to the great S_{BET} and mesoporous pores, which is conducive to the diffusion of I_3^- ions and the contribution of N doping is that the provision of a large number of defect sites, contributes to the increase in charge transfer, which ultimately ensures the electrocatalytic activity of Ni@NPC-1.5 for reducing I_3^- ions.

To more intuitively evaluate the photovoltaic performance of the biomass-blueberry composites as CEs for DSSCs, the PCE values of other biomass-derived carbons were compared. As shown in Table 3, the PCE value (4.86%) of the blueberry-based CEs assembly was higher than or not significantly different from that previously reported for biomass carbon-based CEs (PCE = 1.89–5.54%). In this experiment, through the synergistic effect of KOH activation and melamine, the specific surface area of the blueberry carbon-based material was increased, making it exhibit excellent electrocatalytic activity.

3.4 Analysis of the electrochemical performance of Ni@NPC-1.5

Ni@NPC-1.5 exhibits a nearly rectangular and well-symmetrical *CV* curve even with an increased scan rate (Fig. 10a). As can be seen from Fig. 10b, the potential varies linearly with time and has a symmetrical triangle shape. Observing the GCD curve, almost

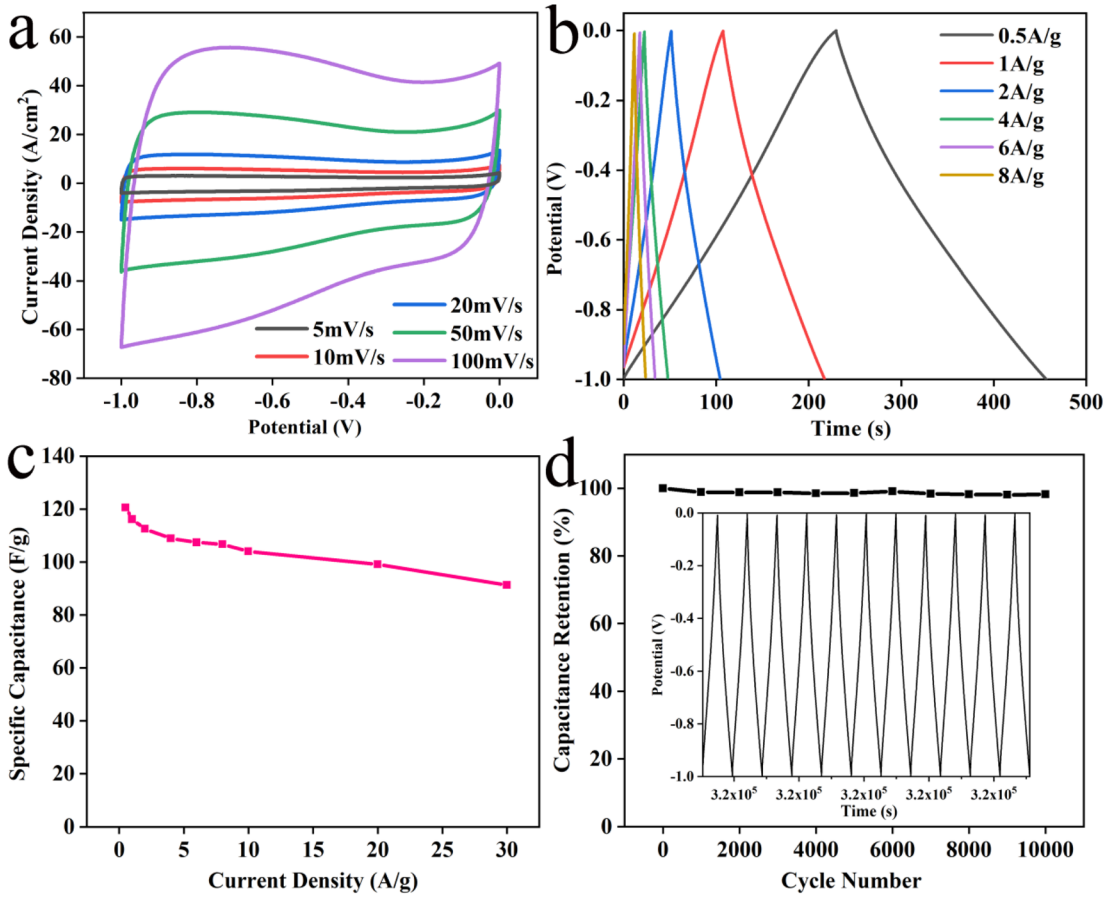

Fig. 10 *CV* curves (a) of Ni@NPC-1.5, GCD curves (b), specific capacitance values (c), cycling performance for the Ni@NPC-1.5 at 6 A g^{-1} over 10 000 cycles (d).

no voltage drop was observed, indicating that the electrode has a low internal resistance, can be charged/discharged quickly, and has good rate performance. The specific capacitance of Ni@NPC-1.5 is 120.55, 116.12, 112.46, 108.88, 107.37, 106.66, 103.94, 99.02, and 91.27 F g^{-1} at 0.5, 1, 2, 4, 6, 8, 10, 20 and 30 A g^{-1}, respectively (Fig. 10c). The cycling stability shown in Fig. 10d represents a good capacitance retention of 98.2% after 10 000 cycles. So, the above analysis further provides a basis for supporting the good electrochemical stability and reversibility of Ni@NPC-1.5 from an electrochemical point of view.

4 Conclusions

In the current work, the P25/blueberry anthocyanin (P25/PBP, photoanode) composite material and the blueberry-derived N-doped porous carbon-loaded Ni nanoparticle composite material (Ni@NPC-*X*, CE) served as two functional electrodes for the fabrication of blueberry-based DSSCs and their characteristics and performance were evaluated. When the masses of anthocyanins introduced into P25 were 0.025 g, 0.05 g, 0.1 g, and 0.2 g, different PCE values of 5.46%, 5.82%, 5.63%, and 4.11%, respectively, were observed. Among them, the PCE was the highest (5.82%) with the addition of 0.05 g of anthocyanin, which is higher than that with pure P25 (4.96%). According to electrochemical and UV-visible results, the combination of PBP and TiO_2 reduces charge recombination and improves the dye adsorption capacity of the photoanode. In addition, by adding 1 g, 1.5 g, and 2 g of melamine, N-doped porous carbon materials loaded Ni nanoparticle composites (Ni@NPC-1, Ni@NPC-1.5, and Ni@NPC-2) were constructed. Melamine changes the microscopic morphology of bio-based materials into petals and increases the S_{BET}. In the Ni@NPC-*X* composite, PC with a porous three-dimensional network structure was used as the electrocatalytic Ni carrier material to reduce the agglomeration of Ni nanoparticles. Ni@NPC-1.5 showed excellent electron transfer ability in electrochemistry with a lower R_{ct} of 3.02 Ω than that of Pt (R_{ct} of 4.91 Ω). The PCE values of the DSSCs fabricated by Ni@NPC-1, Ni@NPC-1.5, and Ni@NPC-2 composite materials as the counter electrode and P25/PBP as the photoanode were 3.88%, 4.86%, and 2.99%, respectively. Among them, the PCE of DSSCs with Ni@NPC-1.5 as CE (4.86%) was the highest close to that of Pt as CE (5.82%). Moreover, from an electrochemical point of view, it provides the basis for supporting the good electrochemical stability and reversibility of Ni@NPC-1.5. The reported blueberry electrode material not only improved the electrochemical performance of the photoanode but also showed a performance close to that of Pt as the counter electrode, which provided new ideas for blueberries-based photovoltaic-electric energy systems for DSSCs.

Conflicts of interest

There are no conflicts to declare.

Acknowledgements

This work was supported by the Innovation Project of Guangxi Graduate Education (YCSW2022003), the National Innovation and Entrepreneurship Training Plan for College Students of Guangxi University (202110593103), and the National Natural Science Foundation of China (Grants No. 31960293).

References

1 B. Li, L. Wang, B. Kang, P. Wang and Y. Qiu, *Sol. Energy Mater. Sol. Cells*, 2006, **90**, 549–573.
2 M. Feng, S. You, N. Cheng and J. Du, *Electrochim. Acta*, 2019, **293**, 356–363.
3 W. Yang, Y. Yao, P. Guo, H. Sun and Y. Luo, *Phys. Chem. Chem. Phys.*, 2018, **20**, 29866–29875.
4 J. Wu, Z. Lan, J. Lin, M. Huang, Y. Huang, L. Fan, G. Luo, Y. Lin, Y. Xie and Y. Wei, *Chem. Soc. Rev.*, 2017, **46**, 5975–6023.
5 J. M. K. W. Kumari, G. K. R. Senadeera, M. A. K. L. Dissanayake and C. A. Thotawatthage, *Ionics*, 2017, **23**, 2895–2900.
6 Y. Jo, J. Y. Cheon, J. Yu, H. Y. Jeong, C. H. Han, Y. Jun and S. H. Joo, *Chem. Commun.*, 2012, **48**, 8057–8059.
7 J. Zhou, L. Chen, Y. Wang, Y. He, X. Pan and E. Xie, *Nanoscale*, 2016, **8**, 50–73.
8 P. Makal and D. Das, *Mater. Chem. Phys.*, 2021, **266**, 124520.
9 N. Gao, T. Wan, Z. Xu, L. Ma, S. Ramakrishna and Y. Liu, *Mater. Chem. Phys.*, 2020, **255**, 123542.
10 J. Wang, X. Nie, W. Wang, Z. Zhao, L. Li and Z. Zhang, *Optik*, 2021, **242**, 167245.
11 D. Lu, L. Qin, D. Liu, P. Sun, F. Liu and G. Lu, *Electrochim. Acta*, 2018, **292**, 180–189.
12 I. Ahmad, R. Jafer, S. M. Abbas, N. Ahmad, R. Ata ur, J. Iqbal, S. Bashir, A. A. Melaibari and M. H. Khan, *J. Alloys Compd.*, 2022, **891**, 162040.
13 T. Alizadeh, F. Zargar and M. R. Zamanloo, *J. Mater. Sci.: Mater. Electron.*, 2019, **30**, 7981–7991.
14 M. Batmunkh, M. Dadkhah, C. J. Shearer, M. J. Biggs and J. G. Shapter, *Appl. Surf. Sci.*, 2016, **387**, 690–697.
15 P. Zhang, C. L. Shao, Z. Y. Zhang, M. Y. Zhang, J. B. Mu, Z. C. Guo and Y. C. Liu, *Nanoscale*, 2011, **3**, 2943–2949.
16 S. N. Yun, Y. W. Zhang, Q. Xu, J. M. Liu and Y. Qin, *Nano Energy*, 2019, **60**, 600–619.
17 G. T. Yue, L. Wang, X. A. Zhang, J. H. Wu, Q. W. Jiang, W. F. Zhang, M. L. Huang and J. M. Lin, *Energy*, 2014, **67**, 460–467.
18 Y. Zhang, Y. Jiao, M. Liao, B. Wang and H. Peng, *Carbon*, 2017, **124**, 79–88.
19 H. M. Chuang, C. T. Li, M. H. Yeh, C. P. Lee, R. Vittal and K.-C. Ho, *J. Mater. Chem. A*, 2014, **2**, 5816–5824.
20 R. Tas, M. Can and S. Sonmezoglu, *IEEE J. Photovolt.*, 2017, **7**, 792–801.
21 W. Hou, Y. Xiao and G. Han, *Angew. Chem., Int. Ed.*, 2017, **56**, 9146–9150.
22 J. Li, S. Yun, F. Han, Y. Si, A. Arshad, Y. Zhang, B. Chidambaram, N. Zafar and X. Qiao, *J. Colloid Interface Sci.*, 2020, **578**, 184–194.
23 A. A. Qureshi, S. Javed, H. M. Asif Javed, A. Akram, M. Jamshaid and A. Shaheen, *Opt. Mater.*, 2020, **109**, 110267.

24 J. Qiu, D. He, H. Wang, W. Li, B. Sun, Y. Ma, X. Lu and C. Wang, *Electrochim. Acta*, 2021, **367**, 137451.
25 T. K. Das, P. Ilaiyaraja and C. Sudakar, *Sol. Energy*, 2018, **159**, 920–929.
26 Z. Shen, G. Wang, H. Tian, J. Sunarso, L. Liu, J. Liu and S. Liu, *Electrochim. Acta*, 2016, **216**, 429–437.
27 B. Yu, A. Gele and L. Wang, *Int. J. Biol. Macromol.*, 2018, **118**, 478–484.
28 K. Zou, Y. Deng, J. Chen, Y. Qian, Y. Yang, Y. Li and G. Chen, *J. Power Sources*, 2018, **378**, 579–588.
29 Y. Liu, X. Li, Y. Li, Z. Zhao and F. Bai, *Appl. Phys. A*, 2016, **122**, 174.
30 Y. Shang, X. Liu, J. Zhang, C. Lu and C. Zhang, *Ionics*, 2021, **27**, 1967–1976.
31 K. Mi, S. Chen, B. Xi, S. Kai, Y. Jiang, J. Feng, Y. Qian and S. Xiong, *Adv. Funct. Mater.*, 2017, **27**, 1604265.
32 B. Chai, T. Peng, P. Zeng and J. Mao, *J. Mater. Chem.*, 2011, **21**, 14587.
33 R. Yuan, H. Wen, L. Zeng, X. Li, X. Liu and C. Zhang, *Nanomaterials*, 2021, **11**, 694.
34 Q. Wu, W. Li, J. Tan, Y. Wu and S. Liu, *Chem. Eng. J.*, 2015, **266**, 112–120.
35 Y. Zhao, J. Shen, Z. Yu, M. Hu, C. Liu, J. Fan, H. Han, A. Hagfeldt, M. Wang and L. Sun, *J. Mater. Chem. A*, 2019, **7**, 12808–12814.
36 W. M. Yin, L. F. Tian, B. Pang, Y. R. Guo, S. J. Li and Q. J. Pan, *Int. J. Biol. Macromol.*, 2020, **156**, 988–996.
37 A. Shrestha, M. Batmunkh, C. J. Shearer, Y. Yin, G. G. Andersson, J. G. Shapter, S. Qiao and S. Dai, *Adv. Energy Mater.*, 2016, **7**, 1602276.
38 S. M. Li, S. Y. Yang, Y. S. Wang, H. P. Tsai, H. W. Tien, S. T. Hsiao, W. H. Liao, C. L. Chang, C. C. M. Ma and C. C. Hu, *J. Power Sources*, 2015, **278**, 218–229.
39 G. Kyriakou, A. M. Márquez, J. P. Holgado, M. J. Taylor, A. E. H. Wheatley, J. P. Mehta, A. E. Fraser, J. Fernández Sanz, S. K. Beaumont and R. M. Lambert, *ACS Catal.*, 2019, **9**, 9310–9310.
40 R. Ghayoor, A. Keshavarz, M. N. S. Rad and A. Mashreghi, *Mater. Res. Express*, 2018, **6**, 025505.
41 A. Hegazy, N. Kinadjian, B. Sadeghimakki, S. Sivoththaman, N. K. Allam and E. Prouzet, *Sol. Energy Mater. Sol. Cells*, 2016, **153**, 108–116.
42 U. Mehmood, M. Zaheer Aslam, R. A. Shawabkeh, I. A. Hussein, W. Ahmad and A. G. Rana, *IEEE J. Photovolt.*, 2016, **6**, 1191–1195.
43 L. Chen, X. Li, Y. Wang, C. Gao, H. Zhang, B. Zhao, F. Teng, J. Zhou, Z. Zhang, X. Pan and E. Xie, *J. Power Sources*, 2014, **272**, 886–894.
44 A. Zaban, M. Greenshtein and J. Bisquert, *Chemphyschem*, 2003, **4**, 859–864.
45 X. Wang, S. Wang, Y. Xie, Y. Jiao, J. Liu, X. Wang, W. Zhou, Z. Xing and K. Pan, *ACS Sustainable Chem. Eng.*, 2019, **7**, 14353–14360.
46 M. Chen, L.-L. Shao, X.-W. Lv, G.-C. Wang, W.-Q. Yang, Z.-Y. Yuan, X. Qian, Y.-Y. Han and A.-X. Ding, *Chem. Eng. J.*, 2020, **390**, 124633.
47 T. Zhang, S. Yun, X. Li, X. Huang, Y. Hou, Y. Liu, J. Li, X. Zhou and W. Fang, *J. Power Sources*, 2017, **340**, 325–336.
48 X. Cui, J. Xiao, Y. Wu, P. Du, R. Si, H. Yang, H. Tian, J. Li, W. H. Zhang, D. Deng and X. Bao, *Angew. Chem., Int. Ed.*, 2016, **55**, 6708–6712.
49 M. Chen, G. C. Wang, L.-L. Shao, Z.-Y. Yuan, X. Qian, Q.-S. Jing, Z.-Y. Huang, D.-L. Xu and S.-X. Yang, *ACS Appl. Mater. Interfaces*, 2018, **10**, 31208–31224.
50 Y. J. Huang, Y. J. Lin, H. J. Chien, Y. F. Lin and K. C. Ho, *Nanoscale*, 2019, **11**, 12507–12516.
51 Y. Zhang, S. Yun, C. Wang, Z. Wang, F. Han and Y. Si, *J. Power Sources*, 2019, **423**, 339–348.
52 Z. Li, L. Zhang, B. S. Amirkhiz, X. Tan, Z. Xu, H. Wang, B. C. Olsen, C. M. B. Holt and D. Mitlin, *Adv. Energy Mater.*, 2012, **2**, 431–437.
53 Y. Di, Z. Xiao, X. Yan, G. Ru, B. Chen and J. Feng, *Appl. Surf. Sci.*, 2018, **441**, 807–815.
54 S. Xu, C. Liu and J. Wiezorek, *Mater. Chem. Phys.*, 2018, **204**, 294–304.
55 G. Wang, D. Wang, S. Kuang, W. Xing and S. Zhuo, *Energy*, 2014, **63**, 708–714.
56 C. Xiang, T. Lv, C. A. Okonkwo, M. Zhang, L. Jia and W. Xia, *J. Electrochem. Soc.*, 2017, **164**, H203–H210.
57 Y. Zhang, S. Yun, Z. Wang, Y. Zhang, C. Wang, A. Arshad, F. Han, Y. Si and W. Fang, *Ceram. Int.*, 2020, **46**, 15812–15821.